

Joint Semi-supervised 3D Super-Resolution and Segmentation with Mixed Adversarial Gaussian Domain Adaptation

Nicolò Savioli^{a,b}, Antonio de Marvao^a, Wenjia Bai^{b,c}, Shuo Wang^b, Stuart A. Cook^d, Calvin W. L. Chin^d, Daniel Rueckert^{b,e}, Declan P. O'Regan^a

^aMRC London Institute of Medical Sciences, Imperial College London, London, UK

^bDepartment of Computing, Imperial College London, London, UK

^cDepartment of Brain Sciences, Imperial College London, London, UK

^dNational Heart Research Institute Singapore, National Heart Center Singapore, Singapore

^eInstitute for Artificial Intelligence and Informatics, Klinikum rechts der Isar, Technical University of Munich, Germany

ARTICLE INFO

Article history:

Keywords: Deep Learning, Super-Resolution (SR), Variational Inference, MRI, Joint Segmentation

ABSTRACT

Optimising the analysis of cardiac structure and function requires accurate 3D representations of shape and motion. However, techniques such as cardiac magnetic resonance imaging are conventionally limited to acquiring contiguous cross-sectional slices with low through-plane resolution and potential inter-slice spatial misalignment. Super-resolution in medical imaging aims to increase the resolution of images but is conventionally trained on features from low resolution datasets and does not super-resolve corresponding segmentations. Here we propose a semi-supervised multi-task generative adversarial network (Gemini-GAN) that performs joint super-resolution of the images and their labels using a ground truth of high resolution 3D cines and segmentations, while an unsupervised variational adversarial mixture autoencoder (V-AMA) is used for continuous domain adaptation. Our proposed approach is extensively evaluated on two transnational multi-ethnic populations of 1,331 and 205 adults respectively, delivering an improvement on state-of-the-art methods in terms of Dice index, peak signal-to-noise ratio, and structural similarity index measure. This framework also exceeds the performance of state-of-the-art generative domain adaptation models on external validation (Dice index 0.81 vs 0.74 for the left ventricle). This demonstrates how joint super-resolution and segmentation, trained on 3D ground-truth data with cross-domain generalization, enables robust precision phenotyping in diverse populations.

© 2022 Imperial College London

1. Introduction

Image super-resolution (SR) is a class of techniques in computer vision that is used to reconstruct a high resolution (HR) image from observed low resolution (LR) images. Improving the details of an image is valuable across a range of natural image applications including data compression (Cao et al., 2020) and feature extraction (Rasti et al., 2016). It is particularly relevant in medical imaging where there are physical constraints

on the acquired spatial resolution and high-resolution structural detail may hold discriminative clinical information (Cui et al., 2014). SR representations are important for cardiac imaging where detailed variations in structure and motion are informative for genetic association studies and prognostic stratification (Bello et al., 2019; Schafer et al., 2017). While acquiring three-dimensional cardiac magnetic resonance (CMR) cine imaging is feasible (Moghari et al., 2018), routine clinical practice and population biobanks are still dominated by multi-slice 2D cine imaging, which limits accurate assessment of geometry due to poor through-plane resolution.

Dictionary-based approaches, such as deformable patch-match methods, aim to recover HR patches from LR images via priors between the target image and training data (Zhu et al., 2014). However, such methods are computationally demanding

as the candidate patches have to be searched to find the most suitable match. In contrast, SR convolutional neural networks learn an end-to-end mapping between LR and HR images, and have significantly improved the quality and efficiency of reconstructions (Gholipour et al., 2010; Sánchez and Vilaplana, 2018; Chaudhari et al., 2018; Chen et al., 2018; Dong et al., 2014). These methods use a convolutional neural network (CNN) that codifies non-linear transformations (i.e., patch extraction, non-linear mapping, and reconstruction) with a combination of ResNet blocks and generative adversarial networks (GANs) (Ledig et al., 2017). Making use of multiple images acquired from different slice directions can further improve and constrain the HR image reconstruction (Oktay et al., 2017; Davatzikos et al., 2003). Lately, optical flow interpolation has been proposed for intensity cardiac image SR (Xia et al., 2021). This method is based on recent advances in the field of video interpolation (Bao et al., 2019), where intermediate sections are synthesized through an optical flow transformation of the cine data. However, the proposed method cannot eliminate slice misalignment and inter-slice motion artifacts (i.e., where differing breath-hold positions during scanning generate imperfect alignment between slices).

These strategies perform segmentation independently of processing the intensity image and do not share the same feature encoder for the related tasks of super-resolving the greyscale image and its semantic label map. Multi-task deep learning approaches with atlas propagation for shape-refined segmentation can produce anatomically smooth models that are robust to the presence of artifacts in the input CMR volumes (Duan et al., 2019). A limitation is the computational cost needed to perform atlas propagation and the output is only HR label maps without an end-to-end super-resolved image. Joint SR and segmentation using GANs (segSR-GAN) have been proposed for brain imaging (Delannoy et al., 2020) as an extension of SR-GAN (Ledig et al., 2017). The segSR-GAN model initially performs both interpolation and patch image subdivisions of the LR input and maps it to an output within two separate up-convolutional layers. However, the initial pre-interpolation step may amplify artifacts such as the motion between successive slices or intensity bias within a given slice. Also, both pre-interpolation and/or patch image subdivisions have long computational times and may not be suitable for clinical applications or large datasets.

In common with other classification tasks, if the training and test images for SR are drawn from different distributions, domain adaptation is needed to reduce sample bias to improve generalization performance across populations (Wang and Deng, 2018). There are three main techniques for domain adaptation: divergence-based domain adaptation, adversarial-based domain adaptation, and reconstruction-based domain adaptation (Shui et al., 2020; Hoffman et al., 2018; Yang et al., 2020). The divergence-based domain adaptation method works by minimizing a divergence criterion between source and target distributions for achieving domain invariant feature representation. In adversarial-based domain adaptation, a synthetic target data domain is generated from the source data by applying GANs. A domain confusion loss is alternately applied to balance the distributions of the source and target domain in one shot within a confusion metric in the final regression layer (Tzeng et al.,

2014). Finally, in the reconstruction-based domain adaptation approach, a shared representation of the domain simultaneously solves classification and reconstruction maintaining information in the target domain (Ghifary et al., 2016). However, the adversarial-based domain adaptation is the most used method in the medical field (Perone et al., 2019; Dou et al., 2018), but is still prone to mode collapse (Durall et al., 2020) that leads the domain adaption model to collapse in the wrong distribution. The variational adversarial autoencoder model proposed here has two main advantages: it solves the mode collapse problem by decoupling the distribution transformation within two variational networks and, at the same time, simplifies the mapping operation between source and target distributions.

In this work, we propose: i) a generative adversarial network called Gemini-GAN that jointly performs SR of greyscale cine images and their label maps and (ii) a generative domain adaptation approach (Variational Adversarial Mixture Autoencoder, V-AMA) which together with joint SR, generalizes across different populations. This approach enforces cross-domain consistency and benefits from complementary learning of super-resolving images and their segmentations. In contrast to previous work, we use a natively HR ground truth for training and validate our approach on two independent multi-ethnic cardiac MR datasets.

2. Datasets

We used paired natively acquired LR/HR images and their respective segmentations for model training, taking advantage of the near-isotropic HR 3D cine datasets available in the UK Digital Heart Project (UKDHP). We then generalized the model to an external population with equivalent paired LR/HR data available (National Heart Center Singapore Biobank), and then to a further population with only LR data available (UK Biobank) which is an intended use case. Table 1 summarizes the phenotypic characteristics of the datasets used. Images were stored on an open-source database (MRIdb, Imperial College London, UK) (Woodbridge et al., 2013). Ground truth labels for both LR and HR datasets were derived as previously described (Bai et al., 2015). In each case ethical approval and written informed consent was obtained.

2.1. UK Digital Heart Project (UKDHP)

A dataset of 1331 healthy adults was used from the UK Digital Heart Project at Imperial College London. High-spatial resolution 3D balanced steady-state free precession cine sequences were used that assessed the left and right ventricles in their entirety in a single breath-hold (60 sections, reconstructed voxel size $1.2 \times 1.2 \times 2$ mm, 20 cardiac phases, typical breath-hold 20s). Conventional single slice multi-breath-hold images were also acquired in the same geometry (10 sections, reconstructed voxel size $1.8 \times 1.8 \times 8$ mm). Imaging was performed on a 1.5-T Philips Achieva system (Best, the Netherlands).

2.2. National Heart Center Singapore Biobank (SG)

External validation was performed on a dataset of 205 healthy adults recruited to the National Heart Center Singapore Biobank

using the same LR/HR image acquisition parameters as the UKDHP but obtained on a 1.5T Aera (Siemens Healthcare, Erlangen, Germany).

2.3. UK Biobank (UKBB)

Generalisation to a second external dataset with only LR cine images was performed in 1331 adults prospectively recruited to UK Biobank (Bycroft et al., 2018). Conventional LR conventional single slice multi-breath-hold images were acquired (10 sections, reconstructed voxel size $1.8 \times 1.8 \times 8$ mm) performed to a standard protocol on a 1.5T Aera (Siemens Healthcare, Erlangen, Germany) (Petersen et al., 2015). Data was processed under access number 40616.

| Characteristic | UKDHP (n=1,331) | SG (n=205) | UKBB* (n=1,331) |
|----------------|--------------------|---------------|--------------------|
| Age (years) | 37.7 ± 12.51 | 50.2 ± 14.69 | 56.5 ± 8.1 |
| Sex (male) | 578.0 (43.4%) | 106 (51.7%) | 86.7 (54.9%) |
| Ethnicity | | | |
| Caucasian | 922.0 (69.3%) | - | 150.4 (95.2%) |
| Chinese | - | 191 (93.17%) | - |
| South Asian | 180 (13.5%) | 11 (5.3%) | - |
| African | 145 (10.9%) | - | - |
| Other | 84 (6.3%) | 3 (1.4%) | - |
| BSA (m^2) | 1.8±0.2 | 1.7±0.2 | 1.9±0.22 |
| SBP ($mmHg$) | 118.3±14.3 | 134.4±18 | 139.7±19.6 |
| DBP ($mmHg$) | 77.9±9.5 | 80.1±11.6 | 82.2±10.7 |

Table 1: Population characteristics. Values are n (%) or mean ± standard deviation. * Characteristics shown for whole population. SG, Singapore biobank; UKDHP, UK Digital Heart Project; UKBB, UK Biobank; BSA, body surface area; SBP, systolic blood pressure; DBP, diastolic blood pressure.

3. Methods

Here we describe the proposed Gemini-GAN for joint super-resolution of greyscale images and segmentation labels from routine 2D cine sequences. We then describe how V-AMA uses a novel domain transfer technique to map a source distribution to the target distribution where Gemini-GAN was previously trained. The whole framework combines both methods (V-AMA and Gemini-GAN) and enables joint SR to be generalised across domains.

3.1. Gemini-GAN model

The proposed Gemini-GAN (Fig. 1) is based on the UNet style model (Ronneberger et al., 2015), and consists of one encoder path and two decoder paths (i.e., one for SR and one for segmentation reconstruction). The encoder path is composed of repeated 3×3 convolutions, followed by a Rectified Linear Unit (ReLU) and a Batch Normalisation (BN) layer. The twin’s decoder branches are made by up-convolutions concatenated with the corresponding cropping feature maps from the decoder path. The networks take as input a 2D stack of LR slices $d \times w \times h$, where d is the number of slices along the z-axis and $w \times h$ is the size of each cardiac slice. The input channels

d of the network are equal to the size of the z axis’s input volume. The feature maps in the latent space are split into two decoders: one for reconstructing the SR greyscale image and one for the 3D segmentation. Each feature map of each decoder layer is concatenated to the upsampling layer for both SR and 3D segmentation through skip path connections. We refer to this network as Generator G_{Gemini} . The energy function for the segmentation encoder branch of G_{Gemini} is a cross-entropy criterion that combines log-softmax and log-likelihood.

The log softmax [Eq. 1] takes as input a 3D dimensional input.

$$p_f(x) = \frac{e^{z_f(x)}}{\sum_{i=1}^K e^{z_i(x)}} \quad (1)$$

Here $z_d(x)$ in the numerator denotes the activation map at the feature channel f and pixel position $x \in \mathbb{R}^2$ for each cardiac slice. While the sum of the denominator is a normalization across K segmentation class and ensures that the sum of probability components in the output vector $p_f(x)$ are equal. A Cross Entropy (CE_{Loss}) loss is then defined as the log-likelihood of probability of log-softmax distribution $p_f(x)$. The weight map $w_f(x)$ assigning importance to each segmentation K class pixel as follows:

$$CE_{Loss} = w_f(x) \cdot \log(p_f(x)) \quad (2)$$

Instead in the SR reconstruction branch a Mean Square Error (MSE) is used:

$$MSE_{Loss} = \frac{1}{n} \sum_{i=1, j=1}^n (o_{i,j} - y_{i,j})^2 \quad (3)$$

The $o_{i,j}$ is the output from the SR decoder and $y_{i,j}$ the corresponding SR ground truth, n is the number of image pixels $[i, j]$.

The L2 penalty loss is then defined as the square root of MSE :

$$L2_{Loss} = \beta \cdot \sqrt{(o_{i,j} - y_{i,j})^2} = \beta \cdot \sqrt{n MSE_{Loss}} \quad (4)$$

To increase the performance of the network an SR discriminator D_{SR} is also coupled which corresponds to a network formed by eight 3×3 reiterated convolutions followed by BN and LeakyReLU with a threshold value set at 0.2. The generator network G_{Gemini} maps the LR volume as a “fake” greyscale SR and 3D segmentation volumes. The concatenation operation (+) is applied to both “fake”-generated volumes sampling by $I_{fake}^{SR} \sim (I_{seg}^{SR} + I_{grey}^{SR})$ where I_{seg}^{SR} and I_{grey}^{SR} are outputs of G net. Then, the concatenation I_{fake}^{SR} is sent to the SR discriminator D_{SR} [Fig. 1] trained to distinguish it from the corresponding “real”-dataset concatenation $I_{real}^{SR} \sim (I_{seg}^{SR} + I_{grey}^{SR})$ of greyscale SR and 3D segmentation sampling from training dataset distribution. The final GAN loss is formulated as follows:

$$\begin{aligned} GAN_{Loss} &= \min_G \max_{D_{SR}} L_{GAN_{Gemini}}(D_{SR}, G) = \\ &= \mathbb{E}_{I_{real}^{SR} \sim UKDHP(I_{seg}^{SR} + I_{grey}^{SR})} [\log(D_{SR}(I_{real}^{SR}))] + \\ &\quad \mathbb{E}_{I_{fake}^{SR} \sim G(I_{seg}^{SR} + I_{grey}^{SR})} [\log(1 - D_{SR}(I_{fake}^{SR}))] \end{aligned} \quad (5)$$

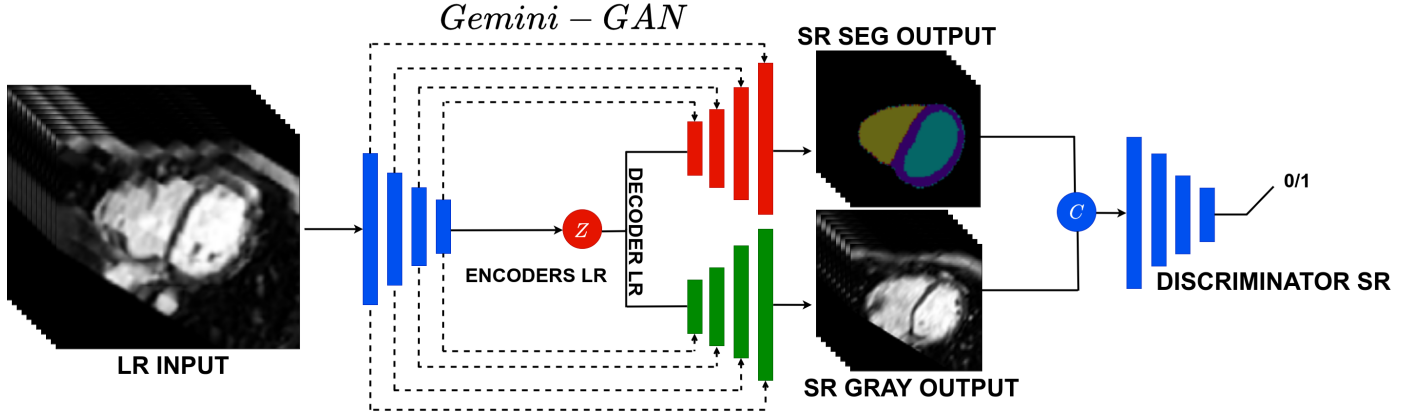


Fig. 1: The figure shows the main components of the proposed G_{Gemini} -GAN model. It is constituted by a (blue) Convolution Neural Network decoder that takes as input the LR volume that is sent into the latent space Z (red), which contains both SR and 3D segmentation latent information. Subsequently, the Z information is sent in two encoder networks constituted by up-convolutions. The first decoder (red) reconstructs the 3D segmentation I_{seg}^{SR} , while the other (green) I_{grey}^{SR} , the volumetric SR images. The dashed lines represent the skip path connections that concatenate the features of each decoder layer with the features of the corresponding upsampling layer. Then these “fake”-generated volumes I_{seg}^{SR} and I_{grey}^{SR} are both concatenated and sent to the SR discriminator to fool it into believing that they are similar to the concatenation of samples from real dataset.

The final joint SR and 3D segmentation loss is a weighted combination of cross-entropy, MSE, GAN, and L2 losses mediated by λ , ω , and β constants:

$$\text{Loss}_{G_{\text{Gemini}}} = CE + \lambda \cdot \text{MSE} + \omega \cdot \text{GAN} + \beta \cdot \text{L2} \quad (6)$$

3.2. Variational Adversarial Mixture Autoencoder (V-AMA)

Here we describe our domain adaption solution. A source domain is defined as $S_d \in \mathbb{R}^3$ and a target domain as $T_d \in \mathbb{R}^3$, where S_d is a LR volume from a specific unknown LR dataset, while T_d is the LR training set volume used by Gemini-GAN. We then train a novel network called Variational Adversarial Mixture Autoencoder (V-AMA) (Fig. 2). The V-AMA network maps an unknown source LR input volume $I_s \in S_d$ to the training target $I_t \in T_d$ LR volume. The V-AMA is composed of three distinct blocks: LR rigid alignment block, variational target network, and variational source mixture network.

3.2.1. Low Resolution Rigid Alignment Block

The LR rigid alignment block allows the alignment between LR source volume of S_d and a target volume of T_d through rigid transformation between them within a set of six landmark points extracted between the apex and base of the ventricles. This simplifies the adaption task; as it only needs to adapt the intensity distribution of the source domain within its target one. The rigid registration process is based on a Singular Value Decomposition (SVD) of the point locations matrix. This method determines the least-squares fit for the distance of the corresponding domain landmarks. Future developments of this block include the automatic prediction of landmarks through a regression neural network and the use of a deep learning algorithm to perform the final rigid transformation. This block is only essential in the training phase to align the target and source volumes and have a correct mapping between them.

3.2.2. Variational Target Network Block

The variational target network block is a deep latent variable generative model for estimating the log-likelihood and the posterior S_t target distribution. The model is composed of an UNet style (Ronneberger et al., 2015) encoder-decoder variational target generator network G_t , followed by a discriminator network D_t . Equivalently, for Gemini-GAN, the decoder path is constituted by 3×3 reiterated convolutions followed by a ReLU and BN. The outputs encoder is made of up-convolutions concatenated with cropped feature maps from the input decoder path. During the training, the variational target generator network G_t (Fig. 2), takes the concatenation of both LR source $I_s \in T_s$ and target volume $I_t \in T_d$ as a batch of 2D slices (i.e., subscript s denotes the source domain and t denotes the target domain).

The input to the target network (i.e., blue encoder in the variational target block 2) is indicated as a concatenation operation (+) between the target volume I_t and source volume I_s to better learn the consistency between both (i.e., $I_i = I_t + I_s$). After the encoding process I_i is mapped to a Gaussian posterior distribution in the latent space $q_\phi(z_t|I_i)_t = \mathcal{N}(z_t; \mu_t, \text{diag}(\sigma_t))$. In particular, ϕ are the variational parameters, z_t the latent variable of the target t encoder, and $I_t \in T_d$ the LR target volume. The following equations explain the variational target encoding (i.e., please refer to theorem Appendix A for more precise mathematical explanation):

$$\begin{aligned} I_i &= I_t + I_s \\ (\mu_t, \log(\sigma_t)) &= \text{Encoding}_{G_\phi}(I_i) \\ q_\phi(z_t|I_i)_t &= \mathcal{N}(z_t; \mu_t, \text{diag}(\sigma_t)) \\ \log(q_\phi(z_t|I_i)_t) &= \sum_k \log(\mathcal{N}(z_{t_k}, 0, 1)) - \log(\sigma_{t_k}) \\ &= \sum_k \frac{1}{2}(\log(\sigma_{t_k}) - \mu_{t_k}^2 - \sigma_{t_k}^2 + 1) \end{aligned} \quad (7)$$

The reconstructed target output I_t^* (i.e., Fig. 2) is concatenated

Variational Adversarial Mixture Autoencoder (V-AMA)

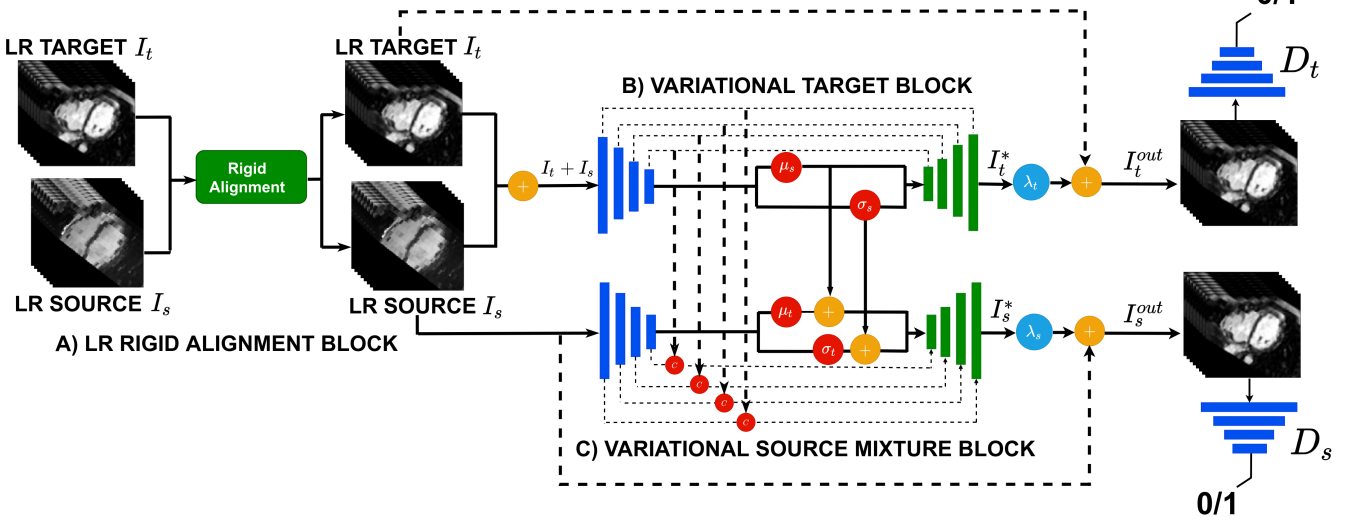


Fig. 2: The figure shows the novel Variational Adversarial Mixture Autoencoder (V-AMA) used for the domain adaption. Particularly, the aim of the network is to adapt the LR information, from an unknown source dataset (i.e., SG, UKBB), to a target one (i.e., UKDHP dataset). The V-AMA model is composed of three distinct blocks: LR rigid alignment block, variational target block, and variational source mixture block. (a) The LR rigid alignment block allows the transformation process through an adaption network we calculated a rigid transformation among them within a set of six landmark points extracted from the apex and base of their respective ventricles. This process is fully automated as we used the respective LR segmentation both for source and target domain volumes. (b) The Variational target block takes input the concatenation of low-resolution target input and low resolution source input (i.e., $I_i = I_t + I_s$) and with network encoder (blue in figure) a posterior target distribution $\log(q_\phi(z_t|I_t))$ (i.e., eq A.11) is estimated. The image output I_t^{out} is reconstructing from (μ_t, σ_t) , where the input target image I_t is added to target output I_t^* . Notably, to enforce the match between the generate target image I_t^{out} and the target volume I_t , a discriminator D_t is used to minimize a GAN loss. (c) Variational source mixture block uses the previous target posterior information (μ_t, σ_t) to move the (μ_s, σ_s) closer the final target distribution.

with I_t in order to constrain the match between the I_i and I_t . The reconstruction target I_t^{out} (in output from the variational target network) is given by:

$$I_t^{out} = I_t + \lambda_t I_t^* \quad (8)$$

where λ_t constant mediates the concatenation between I_t and I_t^* . Also, to better enforce the match between the generated target volume I_t^{out} and the input target volume I_t (i.e., sample from the UKDHP dataset), a discriminator D_t is also used to minimize the following GAN loss for the variational target generator network G_{t_ϕ} (i.e., please also see theorem Appendix B):

$$\begin{aligned} GAN_{Loss}^t &= \min_{G_{t_\phi}} \max_{D_t} L_{GAN_t}(D_t, G_{t_\phi}) = \\ &= \mathbb{E}_{I_t^{real} \sim UKDHP(I_t)} [\log(D_t(I_t^{real}))] + \\ &\quad \mathbb{E}_{I_t^{fake} \sim G_{t_\phi}(I_t)} [\log(1 - D_t(I_t^{fake}))] \end{aligned} \quad (9)$$

Then, the total target loss [Eq. 11], for the variational target network block, is composed by the sum of ELBO loss (i.e., Eq A.6 in the appendix), GAN loss [Eq. 9] and L1 loss. If we rearranging [Eq. A.4, A.5, and A.6] we have:

$$\begin{aligned} VAE_{Loss}_{\theta, \phi}(I_i) &= \log(p_\theta(I_i)) - \log(q_\phi(z_t|I_i) + p_\theta(z_t|I_i)) \\ &= \log(p_\theta(I_i) \cdot p_\theta(z_t|I_i)) - \log(q_\phi(z_t|I_i)) \quad (10) \\ &= p_\theta(I_i, z_t) - \log(q_\phi(z_t|I_i)) \end{aligned}$$

The $p_\theta(I_i, z_t)$ distribution is approximated by a MSE loss between reconstruction target I_t^{out} (i.e., Eq. 8) and variational network input (i.e., $I_i = I_t + I_s$). While the posterior distribution $q_\phi(z_t|I_i)$ is given by the [Eq. A.12] in the appendix.

$$\begin{aligned} VAE_{Loss}_{\theta, \phi}(I_i)_t &= MSE(I_i, I_t^{out}) + \\ &0.5 \cdot \sum_i \frac{1}{2} (\sigma_{t_i}^2 + \mu_{t_i}^2 - \log(\sigma_{t_i}) - 1) \end{aligned} \quad (11)$$

Final target loss (i.e., variational target block in Fig. 2) is:

$$\begin{aligned} Target_{Loss} &= VAE_{Loss}_{\theta, \phi}(I_i) + \\ &L1_{Loss}(I_i, I_t^{out}) + 0.05 * GAN_{Loss}^t \end{aligned} \quad (12)$$

3.2.3. Variational Source Mixture Network Block

After training the variational target block, both encoding features (i.e., at each variational encoding layers) and inference (μ_t and σ_t) [Eq. A.11] are transferred to the source encoder (i.e., indicated with G_{s_ϕ}) to equally inject the same amount of target distribution (Fig.2). The posterior distribution $q_\phi(z_s|I_s)$ (i.e., s in the following equations represent the source domain T_s) is

derived by:

$$\begin{aligned}
 (\mu_s, \log(\sigma_s)) &= \text{Encoding}_{G_{s\phi}}(I_s) \\
 q_\phi(z_s|I_s)_s &= \mathcal{N}(z_s; \mu_s, \text{diag}(\sigma_s)) \\
 \log(q_\phi(z_s|I_s)_s) &= \sum_k \log(\mathcal{N}(z_{s_k}, 0, 1)) - \log(\sigma_{s_k}) \\
 &= \sum_k \frac{1}{2} (\log(\sigma_{s_k}) - \mu_{s_k}^2 - \sigma_{s_k}^2 + 1)
 \end{aligned} \quad (13)$$

where the previous posterior inference of target network $q_\phi(z_t|I_t)_t$ and the new posterior inference of source network $q_\phi(z_s|I_s)_s$ are added together in the latent space of $G_{s\phi}$ to constitute the final mixture KL posterior $q_\phi(z_s|I_s)_m$. Indeed, the source network $G_{s\phi}$ loss is:

$$\begin{aligned}
 \text{VAELoss}_{\theta,\phi}(I_s) &= \text{MSE}(I_s, I_s^{\text{out}}) + \\
 0.5 \cdot \sum_k \frac{1}{2} &(\log(\sigma_{m_k}) - \mu_{m_k}^2 - \sigma_{m_k}^2 + 1)
 \end{aligned} \quad (14)$$

Given that (σ_t, μ_t) and (σ_s, μ_s) are normally distributed independent random variables, then their sum is also normally distributed. Hence, we obtain $\sigma_{m_k}^2$, $\log(\sigma_{m_k})$, $\mu_{m_k}^2$, and z_{m_k} as:

$$\begin{aligned}
 \sigma_{m_k}^2 &= \sigma_{t_k}^2 + \sigma_{s_k}^2 \\
 \log(\sigma_{m_k}) &= \log(\sigma_{t_k}) + \log(\sigma_{s_k}) \\
 \mu_{m_k}^2 &= (\mu_{t_k} + \mu_{s_k})^2 \\
 k_{m_k} &\sim \mathcal{N}(0, I) \\
 z_{m_k} &= (\mu_{t_k} + \mu_{s_k}) + (\sigma_{s_k} + \sigma_{t_k}) \odot k_{m_k}
 \end{aligned} \quad (15)$$

The reconstruction target I_s^{out} in output from $G_{s\phi}$ is given by:

$$I_s^{\text{out}} = I_s + \lambda_s \hat{I}_s^* \quad (16)$$

Where λ_s constant mediates the interaction between the source network input I_s and the output I_s^* . As for $G_{t\phi}$, to better enforce the match between the generated source volume I_s^{out} and the target volume distribution I_t (i.e., sample from the UKDHP dataset), we used a discriminator D_s to minimize the following GAN loss for the $G_{s\phi}$ network:

$$\begin{aligned}
 \text{GAN}_{\text{Loss}}^s &= \min_{G_{t\phi}} \max_{D_s} L_{\text{GAN}_s}(D_s, G_{s\phi}) = \\
 &= \mathbb{E}_{I_t^{\text{real}} \sim \text{UKDHP}(I_t)} [\log(D_s(I_t^{\text{real}}))] + \\
 &\quad \mathbb{E}_{I_s^{\text{fake}} \sim G_{s\phi}(I_s)} [\log(1 - D_s(I_s^{\text{fake}}))]
 \end{aligned} \quad (17)$$

The total source loss, for the variational source network block, is composed by the sum of posterior mixture KL loss (i.e., eq 14 and 15), GAN loss [Eq 17] and L1 loss.

$$\begin{aligned}
 \text{Source}_{\text{Loss}} &= \text{VAELoss}_{\theta,\phi}(I_s) + \\
 \text{L1}_{\text{Loss}}(I_s, I_s^{\text{out}}) &+ 0.05 * \text{GAN}_{\text{Loss}}^s
 \end{aligned} \quad (18)$$

The variational source mixture network uses the target posterior information to fully incorporate the target distribution in

source one so that the source reconstruction I_s^{out} will look like the target image UKDHP style. The obvious benefit is linked to a better inference task in the domain adaption process where the variational target network is only involved to find the posterior distribution that captures the UKDHP style. However, in order to optimize the inference speed, the LR rigid alignment block is used only during the training stage where during test inference both variational target and variational source mixture networks take in input the source I_s .

3.3. Training details

The number of UKDHP patients utilized for training is 1131 with 100 epochs iterations until convergence and finally valid and testing in 100 UKDHP's patients. Data argumentation was also applied through the extraction of random cropping, within vertical and horizontal flip; where the final inference is performed for all networks comparison on the entire volume at LR. The learning rate (lr) used is $1e-4$ with a weight decay (i.e., L2 penalty) of β set to $1e-6$ [Eq 4]. Also the $\lambda = 1$, for giving equal importance to SR than 3D segmentation during the training; while the GAN constant is set to $\omega = 1e-3$. The LR images, and their corresponding segmentation and SR images, are used to train the network in a supervised way with ADAM optimization with random horizontal and vertical flipping and random cropping (Kingma and Ba, 2014). While for V-AMA an ADAM optimization is also used with an lr of 0.0002 and a momentum (i.e., β_1) of 0.5 where $\lambda_t = 1$ and $\lambda_s = 1$. All networks were consistently compared in inference using the full cardiac LR-volume (i.e., no initial cropping and/or interpolation) inputs where the training hyperparameters were kept constant for all training phases. The GPU used is an NVIDIA V100 with a smaller batch size for minimizing the overhead between the GPU and the Hard Disk Drive (HDD) and maximizing the use of the overall deep-learning system.

4. Results

First we describe the metrics used to quantify algorithm performance. We then compare the performance of Gemini-GAN (i.e., super-resolution performances) to several benchmark algorithms used for either sequential or joint SR and segmentation tasks, and then evaluate V-AMA (i.e., domain-adaption performances) in an external dataset against other domain adaptation methods.

4.1. Segmentation and image quality metrics

4.1.1. Dice Index (DI)

Segmentation performance is evaluated for the left ventricular (LV) cavity, LV myocardium and right ventricular (RV) cavity both in end-systole (ED) and end-diastole (ED) with the Dice Index (DI). Given two sets of binary mask X and Y, the DI is defined by the following equation:

$$\text{Dice} = \frac{2|X \cap Y|}{|A| + |B|} \quad (19)$$

Here $|X|$ and $|Y|$ represent the number of elements for X and Y.

4.1.2. Peak Signal-to-Noise Ratio (PSNR)

The PSNR represents the ratio between the maximum possible power of a signal and the power of corrupting noise that affects the fidelity of its representation. The mathematical definition of PSNR is expressed logarithmically. Given two images I and K of size $m \times n$ we define PSNR (in decibel scale) as:

$$\begin{aligned} PSNR &= 10 \cdot \log_{10}\left(\frac{I_{Max}^2}{MSE_{I,K}}\right) = \\ &20 \cdot \log_{10}\left(\frac{I_{Max}}{\sqrt{MSE_{I,K}}}\right) = 20 \cdot \log_{10}(I_{Max}) \\ &\quad - 10 \cdot \log_{10}(MSE_{I,K}) \end{aligned} \quad (20)$$

Here I_{Max} is the maximum possible value of the image I , while $MSE_{I,K}$ is the Mean Squared Error between the image I and K .

$$MSE_{I,K} = \frac{1}{m \cdot n} \sum_{i=0}^{m-1} \sum_{j=0}^{n-1} [I(i, j) - K(i, j)]^2 \quad (21)$$

4.1.3. Structural Similarity Index Measure (SSIM)

The structural similarity index measure (SSIM) is a metric for the assessment of the visual quality of images. Structural information measures the pixel inter-dependencies that emphasize visual structure and take into consideration contrast and luminance (Wang et al., 2004). Given two images x and y of size $m \times n$ the SSIM index is defined as:

$$SSIM(x, y) = \frac{(2\mu_x\mu_y + c_1) \cdot (2\sigma_{xy} + c_2)}{(\mu_x^2 + \mu_y^2 + c_1) \cdot (\sigma_x^2 + \sigma_y^2 + c_2)} \quad (22)$$

Here μ_x is the average of image x , μ_y is the average of image y , σ_x^2 is the variance of image x , σ_y^2 is the variance of image y , and σ_{xy} the covariance of image x and y . The constants c_1 and c_2 stabilize the division in the case of a weak denominator.

4.2. Deep-learning methods comparison

We used three state-of-the-art methods for both SR and segmentation comparison: UNet, SR-GAN, and SegSR-GAN. The UNet model is an advanced segmentation model (Ronneberger et al., 2015) based on an encoding path, that captures the general context of the input image, and a decoding path that produces the final segmentation. While the SR-GAN is based on two networks a ResNet He et al. (2015) generator with a GAN discriminator (i.e., similar to Gemini-GAN). Lastly, the SegSR-GAN (DeLannoy et al., 2020) model, a leading-edge joint segmentation method, is further compared. The SegSR-GAN is essentially similar to SR-GAN in architecture with the exception of having an upsampling block that gives both segmentation and SR outputs. However, to be fully consistent with other model's comparisons (i.e., UNet, SR-GAN, and Gemini-GAN), no initial interpolation and/or image patch extraction was performed to the input (i.e., as in the original paper the SegSR-GAN). We instead prefer to respect the initial architecture proposed by SR-GAN (i.e., adding a skip connection from the first convolution block to the last before the upsampling layer).

4.3. Performance for Super-resolution

We evaluate the super-resolution performances through two main methods: (i) classic interpolation-based methods, (ii) deep learning approaches in the UKDHP dataset which contains paired LR and HR ground truth (Table 2). An example of the output from Gemini-GAN is shown in Figs. 3 and 4. The first three classic interpolation-based methods models evaluated were nearest neighbor (NN), linear, and B-spline which are all sub-optimal both in terms of 3D Segmentation and SR (and they cannot be used for an initial pre-interpolation as in SegSR-GAN paper). The performance of UNet (Ronneberger et al., 2015) for SR and segmentation shows good performance in either task individually. We also show that the SegSR-GAN joint algorithm under-performs the proposed Gemini-GAN model which generally has the highest segmentation accuracy across all comparisons while achieving comparable super-resolved image quality to disjoint methods. As segSR-GAN is a direct derivation of SR-GAN we hypothesize that the decrease in performance for both networks is linked to two main causes: firstly the number of parameters increases with respect to the size of our dataset especially when the ResNet (He et al., 2015) backbone is used. Secondly, the lack of skip-path connections in the upsampling layers causes a loss of high-level information responsible for shape and object detection. The number of ResNet layers utilized does not decisively influence the network performance (i.e., since an data argumentation mechanism, allows to prevent overfitting due to extra network parameters).

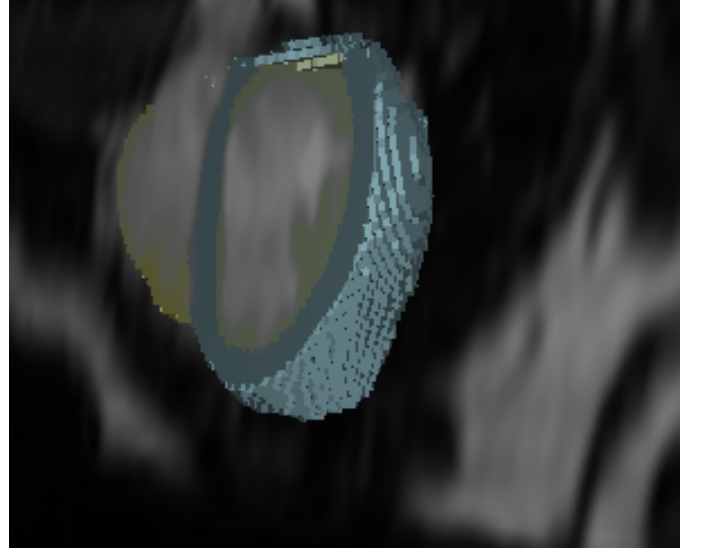


Fig. 3: Joint 3D super-resolution and segmentation of the left and right ventricles cavity in long axis cross-section using the Gemini-GAN network showing the consistency between super-resolved greyscale images and labels prediction.

4.4. Performance for domain adaptation

Here we present the performance of the V-AMA network in the external validation (SG) dataset. Three state-of-the-art networks (CycleGAN (Zhu et al., 2017a), BicycleGAN (Zhu et al., 2017b), and MUNIT (Huang et al., 2018)) used for image domain adaption are compared to V-AMA (Table 3 and Fig.6).

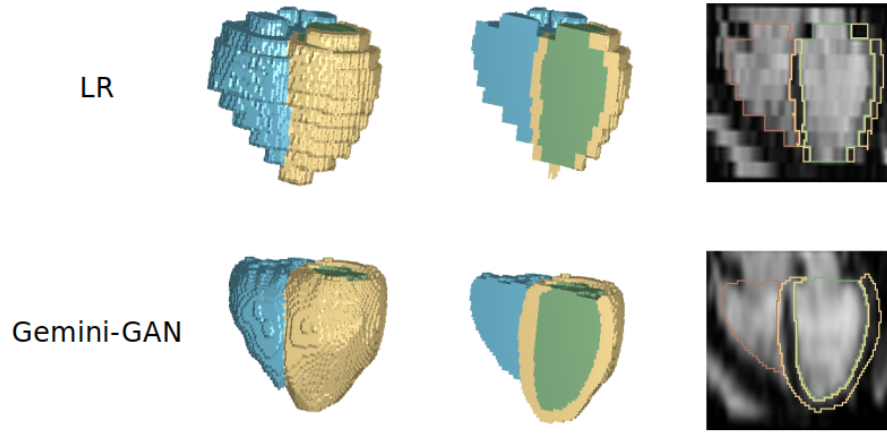


Fig. 4: Three dimensional renderings of the surface and long-axis of the heart (yellow: left ventricular myocardium; green: left ventricular cavity; blue: right ventricular cavity) with corresponding greyscale images and segmentation contours in a long axis reconstruction. A comparison is shown between the acquired low resolution (LR) images and Gemini-GAN’s joint 3D segmentation and super-resolution.

| Metric | Dice | | | | | | PSNR | | SSIM | |
|--|-------------------|-------------------|-------------------|-------------------|-------------------|-------------------|--------------------|--------------------|-------------------|-------------------|
| | LV cavity ED | LV cavity ES | LV myocardium ED | LV myocardium ES | RV cavity ED | RV cavity ES | ED | ES | ED | ES |
| Anatomy | | | | | | | | | | |
| Linear | 0.02(0.01) | 0.01(0.01) | 0.003(0.002) | 0.004(0.006) | 0.001(0.002) | 0.0008(0.004) | 12.69(0.50) | 12.57(0.46) | 0.46(0.03) | 0.44(0.03) |
| Nearest neighbour | 0.02(0.01) | 0.02(0.009) | 0.004(0.002) | 0.005(0.006) | 0.001(0.002) | 0.0009(0.004) | 12.68(0.50) | 12.55(0.46) | 0.46(0.03) | 0.44(0.03) |
| B-Spline | 0.001(0.00) | 0.001(0.00) | 3.24e-05(0.00) | 9.93e-06(0.00) | 3.84e-05(0.00) | 3.52e-05(0.00) | 13.39(0.52) | 13.41(0.48) | 0.46(0.03) | 0.44(0.03) |
| UNet (Ronneberger et al., 2015) (Only Seg) | 0.84(0.05) | 0.72(0.04) | 0.72(0.04) | 0.72(0.06) | 0.71(0.05) | 0.60(0.06) | - | - | - | - |
| UNet (Ronneberger et al., 2015) (Only Img) | - | - | - | - | - | - | 27.86(0.65) | 28.12(0.71) | 0.90(0.01) | 0.91(0.01) |
| SR-GAN (Ledig et al., 2017) (Only Seg) | 0.85(0.05) | 0.50(0.05) | 0.70(0.04) | 0.58(0.05) | 0.71(0.05) | 0.59(0.07) | - | - | - | - |
| SR-GAN (Ledig et al., 2017) (Only Img) | - | - | - | - | - | - | 23.66(0.37) | 23.53(0.38) | 0.77(0.01) | 0.77(0.01) |
| SegSR-GAN (Delannoy et al., 2020) (Joint) | 0.82(0.05) | 0.70(0.05) | 0.70(0.04) | 0.71(0.04) | 0.72(0.06) | 0.58(0.08) | 19.90(0.36) | 20.10(0.29) | 0.53(0.02) | 0.54(0.01) |
| Gemini-GAN [Our] (Joint) | 0.87(0.05) | 0.69(0.06) | 0.75(0.03) | 0.75(0.04) | 0.74(0.05) | 0.64(0.05) | 26.93(0.59) | 27.12(0.60) | 0.88(0.01) | 0.88(0.01) |

Table 2: A comparison of each super-resolution model showing segmentation accuracy for each cardiac structure (Dice) and greyscale image quality metrics (PSNR and SSIM) with mean and standard deviation (Left ventricle, LV; right ventricle, RV; end diastole, ED; end systole; ES).

| Metric | Dice | | | | | | PSNR | | SSIM | |
|--------------------------------|-------------------|-------------------|-------------------|-------------------|-------------------|-------------------|--------------------|--------------------|-------------------|-------------------|
| | LV cavity ED | LV cavity ES | LV myocardium ED | LV myocardium ES | RV cavity ED | RV cavity ES | ED | ES | ED | ES |
| No Adaptation | 0.01(0.01) | 0.01(0.01) | 0.01(0.01) | 0.01(0.01) | 0.01(0.03) | 0.01(0.02) | 10.68(0.71) | 10.55(0.71) | 0.14(0.09) | 0.13(0.10) |
| CycleGAN (Zhu et al., 2017a) | 0.72(0.06) | 0.31(0.06) | 0.67(0.04) | 0.45(0.05) | 0.63(0.06) | 0.33(0.10) | 23.35(0.46) | 23.50(0.43) | 0.49(0.02) | 0.48(0.02) |
| BicycleGAN (Zhu et al., 2017b) | 0.48(0.06) | 0.09(0.03) | 0.54(0.04) | 0.16(0.04) | 0.50(0.08) | 0.14(0.07) | 22.21(1.13) | 21.67(1.26) | 0.49(0.02) | 0.48(0.02) |
| MUNIT (Huang et al., 2018) | 0.74(0.06) | 0.26(0.06) | 0.66(0.04) | 0.41(0.05) | 0.62(0.06) | 0.32(0.10) | 23.12(0.44) | 22.87(0.42) | 0.49(0.02) | 0.48(0.02) |
| V-AMA [Our] | 0.81(0.05) | 0.40(0.06) | 0.71(0.04) | 0.53(0.06) | 0.64(0.04) | 0.41(0.09) | 25.05(0.52) | 24.80(0.54) | 0.49(0.02) | 0.48(0.02) |

Table 3: A comparison in the external validation set (SG) between the presented V-AMA model and state of art networks (i.e., CycleGAN (Zhu et al., 2017a), BicycleGAN (Zhu et al., 2017b), and MUNIT (Huang et al., 2018)) used for image domain adaption relative to “No Adaptation”. Segmentation accuracy for each cardiac structure (Dice) and greyscale image quality metrics (PSNR and SSIM) with mean and standard deviation are shown. (Left ventricle, LV; right ventricle, RV; end diastole, ED; end systole; ES).

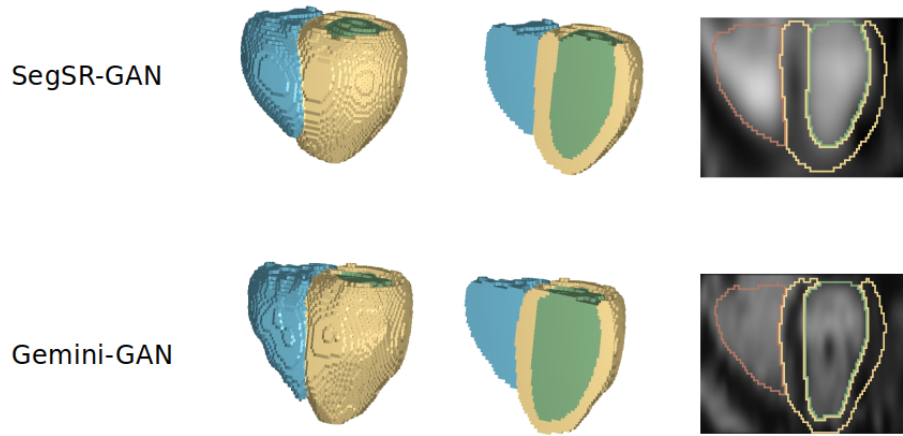


Fig. 5: Three dimensional renderings of the heart comparing Gemini-GAN with the current state-of-the-art for joint segmentation and SR (segSR-GAN (Delannoy *et al.*, 2020)) which does not accurately reconstruct fine anatomic details in the greyscale image.

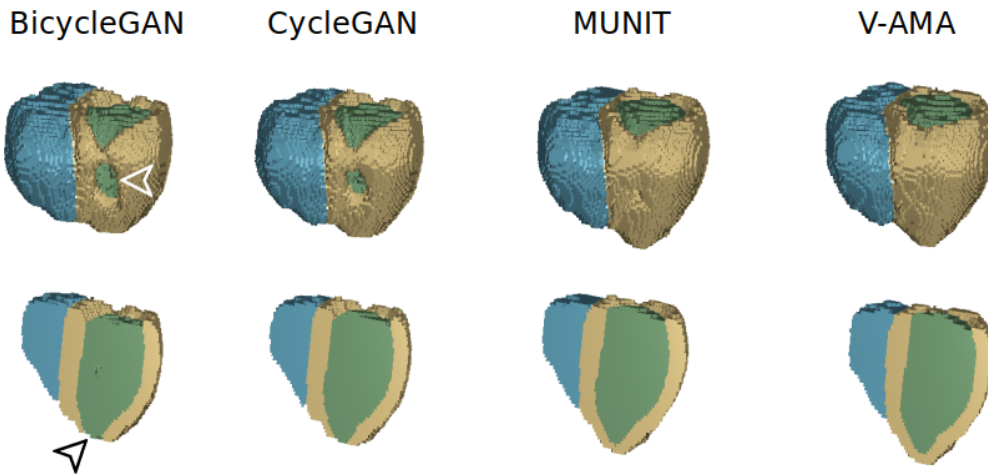


Fig. 6: Three dimensional renderings of the heart comparing 3D segmentations produced by Gemini-GAN after adaptation with different state-of-the-art methods and our proposed V-AMA method. Our proposed framework maintains a complete and smooth geometry of the heart while other methods show discontinuities in the segmentation of the mid-ventricular and apical myocardium (arrowheads).

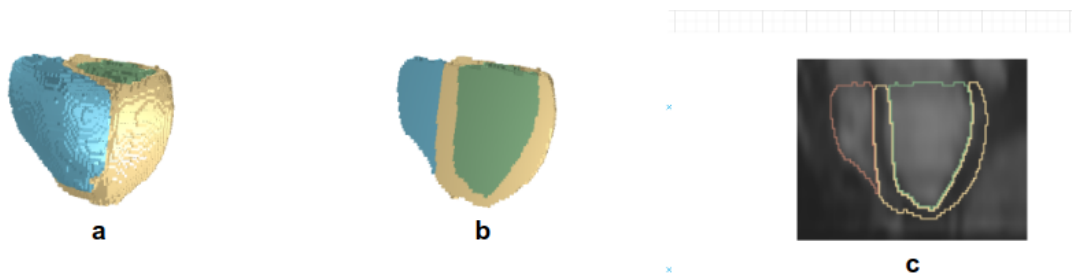


Fig. 7: Three dimensional renderings of the heart comparing demonstrating that our Gemini-GAN + V-AMA framework generalises well to a further external dataset where only LR images are available (UKBB) demonstrating its potential value for routine clinical imaging and biobank samples. a) The full volume reconstruction from the 3D segmentation prediction, b) the volume in cross-section, and c) the grayscale SR with the 3D segmentation contours.

The main goal of CycleGAN is to learn the mapping with a generator from a source distribution to a target one by an adversarial and a cycle consistent loss that boosts the mapping invertibility (Zhu et al., 2017a). To solve this problem, we use BicycleGAN - where two networks are trained with cycle loss and random noise injection. The first network is a conditional variational auto-encoder, that encodes the target image in the latent target space and uses it to map the target image (i.e., from the source image to latent target space to target image). The second network is a conditional latent regressor network and uses the source image and random noise to produce the latent target image (Zhu et al., 2017b). The injection of random noise in the second BicycleGAN network could potentially lead to instability and is reflected by a performance decrease for the Dice index.

In the MUNIT model, the latent space source volume input is decomposed into a style space and content space. This is performed by content encoder and style encoder networks. While the style encoder network is composed of several stride convolutions, followed by global pooling and MPL layer to produce a set of parameters. The content encoder network processes the source volume to give as input to the decoding network with adjusted parameters by the style encoder. However, the style of the content encoder network is limited by the previous global pooling operation in the style encoder that is insufficient to extract detailed information due to the intrinsic limitation of pooling operation (Sabour et al., 2017a) (i.e., pooling takes the neuron with high peak information but not the one relevant for the specific encoding task to performed).

To address this problem, V-AMA is proposed to decouple the source latent space through two adversarial variational networks without any pooling in the style content-encoding where the variational mechanism is instead used to share style information. In the external validation set, this provided the highest segmentation accuracy for all cardiac structures as well as the best image quality metrics.

We further tested V-AMA in the UKBB dataset (which is representative of routine imaging and population data), but since there is no specific SR ground-truth both in 3D segmentation and greyscale in UKBB, we limit our analysis to a qualitative evaluation; confirming the system’s ability to generalize well to a further external dataset (Fig 7).

5. Discussion and Conclusion

The proposed deep-learning system creates a hybrid between supervised and unsupervised learning algorithms for training the Gemini-GAN and V-AMA algorithms respectively. We have shown the improved performance of Gemini-GAN compared to best in class networks for jointly determining 3D Segmentation and SR from a natively LR input volume while maintaining high PSNR and SSIM.

We compared our network with SR-GAN which showed relatively poor performance for segmentation accuracy and image quality. This was primarily due to a lack of a large dataset (i.e., 350,000 ImageNet images were originally used to train SR-GAN) to satisfy the depth of the ResNet networks. Furthermore, the lack of skip path connections in both SR-GAN and

Seg-SRGAN reduces the segmentation performance, as the local information in the high-level features in the first convolutions layers is lost. A further limitation of Seg-SRGAN, is related to the initial input B-spline interpolation which can introduce a prediction bias. Furthermore, interpolating the volume with a classical method, as in the original Seg-SRGAN paper, may be computationally ineffective. This can be unfavorable if we additionally want to determine the spatial information from a full volumetric LR input, where erasing of the skip path, at each up-sampling level, reduces the possibility of reaching the correct 3D spatial information between the individual channels at each encoding layer. However, Gemini-GAN exhibits high performance for both 3D segmentation and SR directly from LR greyscale volumes even with limited dataset size.

Our unsupervised domain adaptation algorithm, V-AMA, is also proposed here. After spatial alignment of the source and target volume within a rigid alignment algorithm, paired distinct adversarial VAE networks are utilized. The first network, called variation target block, extracts the variational source volume parameters in terms of mean and std, transferred to a second network, a variational source mixture block, which mixes both source and target VAE’s parameters. The V-AMA model has several advantages, in the first place it solves the mode collapse problem (Durall et al., 2020), where the optimization of multidimensional non-convex space can lead to instability and collapse the model to a single distribution (i.e., only source but not target). Secondly, it simplifies the mapping operation between source to target distributions by disassociating the inference process within two distinct deep networks. To quantify the ability of V-AMA to adapt its domain in a small dataset we used an external dataset and three modern domain adaption networks demonstrating its accurate and robust performance.

Mode collapse is one of the main problems for other algorithms, which could be partially solved by injecting input noise into the network as in BicycleGAN (Zhu et al., 2017b). The direct injection of random noise in the network could lead to instability especially when the source distribution differs from the target one. Notably, any additional random noise could amplify this behavior. Instead, the MUNIT model decomposes the latent space into style space and content space within two networks decreasing the mode collapse problem. Notably, one of the main limitations of MUNIT is related to global pooling in style encoding, where the global pooling layer loses relevant information and neglecting the spatial relation between the objects in the volume (i.e., LV vs RV cavity position in the volume input) (Sabour et al., 2017b). Instead, our V-AMA model avoids the pooling by mixing the source and target style directly in variational inference fashion.

In summary, we have experimentally demonstrated how our deep learning system can achieve high performance in joint cardiac SR and 3D segmentation tasks with domain adaption to new distributions. Our method will enable future applications in the field of cardiac shape and motion analysis where precision phenotypes are needed for prediction and classification tasks across diverse datasets.

Data availability

The code (Savioli et al., 2021a) and segmentations (Savioli et al., 2021b) used in this study are open access.

Acknowledgments

The study was supported by Bayer AG; Medical Research Council (MC-A658-5QEB0); National Institute for Health Research (NIHR) Imperial College Biomedical Research Centre; British Heart Foundation (NH/17/1/32725, RG/19/6/34387, RE/18/4/34215); Academy of Medical Sciences (SGL015/1006); Mason Medical Research Trust grant; and the Engineering and Physical Sciences Research Council (EP/P001009/1).

References

- Bai, W., Shi, W., de Marvao, A., Dawes, T.J., O'Regan, D.P., Cook, S.A., Rueckert, D., 2015. A bi-ventricular cardiac atlas built from 1000+ high resolution MR images of healthy subjects and an analysis of shape and motion. *Med Image Anal* 26, 133–145.
- Bao, W., Lai, W.S., Ma, C., Zhang, X., Gao, Z., Yang, M.H., 2019. Depth-aware video frame interpolation, in: *Proceedings of the IEEE/CVF Conference on Computer Vision and Pattern Recognition*, pp. 3703–3712.
- Bello, G.A., Dawes, T.J., Duan, J., Biffi, C., de Marvao, A., Howard, L.S., Gibbs, J.S.R., Wilkins, M.R., Cook, S.A., Rueckert, D., et al., 2019. Deep-learning cardiac motion analysis for human survival prediction. *Nat Mach Intell* 1, 95–104.
- Bycroft, C., Freeman, C., Petkova, D., Band, G., Elliott, L.T., Sharp, K., Motyer, A., Vukcevic, D., Delaneau, O., O'Connell, J., et al., 2018. The UK biobank resource with deep phenotyping and genomic data. *Nature* 562, 203–209.
- Cao, S., Wu, C.Y., Krähenbühl, P., 2020. Lossless image compression through super-resolution. *arXiv preprint arXiv:2004.02872*.
- Chaudhari, A.S., Fang, Z., Kogan, F., Wood, J., Stevens, K.J., Gibbons, E.K., Lee, J.H., Gold, G.E., Hargreaves, B.A., 2018. Super-resolution musculoskeletal MRI using deep learning. *Magn Reson Med* 80, 2139–2154.
- Chen, Y., Shi, F., Christodoulou, A.G., Xie, Y., Zhou, Z., Li, D., 2018. Efficient and accurate MRI super-resolution using a generative adversarial network and 3D multi-level densely connected network, in: *International Conference on Medical Image Computing and Computer-Assisted Intervention*, Springer, pp. 91–99.
- Cui, Z., Chang, H., Shan, S., Zhong, B., Chen, X., 2014. Deep network cascade for image super-resolution, in: *European Conference on Computer Vision*, Springer, pp. 49–64.
- Davatzikos, C., Tao, X., Shen, D., 2003. Hierarchical active shape models, using the wavelet transform. *IEEE Trans Med Imaging* 22, 414–423.
- Delannoy, Q., Pham, C.H., Cazorla, C., Tor-Díez, C., Dollé, G., Meunier, H., Bednarek, N., Fablet, R., Passat, N., Rousseau, F., 2020. SegSR-GAN: Super-resolution and segmentation using generative adversarial networks—application to neonatal brain MRI. *Comput Biol Med* 120, 103755.
- Dong, C., Loy, C.C., He, K., Tang, X., 2014. Learning a deep convolutional network for image super-resolution, in: *European conference on computer vision*, Springer, pp. 184–199.
- Dou, Q., Ouyang, C., Chen, C., Chen, H., Heng, P.A., 2018. Unsupervised cross-modality domain adaptation of convnets for biomedical image segmentations with adversarial loss. *arXiv preprint arXiv:1804.10916*.
- Duan, J., Bello, G., Schlemper, J., Bai, W., Dawes, T.J.W., Biffi, C., de Marvao, A., Doumoud, G., O'Regan, D.P., Rueckert, D., 2019. Automatic 3D bi-ventricular segmentation of cardiac images by a shape-refined multi-task deep learning approach. *IEEE Trans Med Imaging* 38, 2151–2164. doi:10.1109/TMI.2019.2894322.
- Durall, R., Chatzimichailidis, A., Labus, P., Keuper, J., 2020. Combating mode collapse in GAN training: An empirical analysis using Hessian Eigenvalues. *arXiv preprint arXiv:2012.09673*.
- Ghifary, M., Kleijn, W.B., Zhang, M., Balduzzi, D., Li, W., 2016. Deep reconstruction-classification networks for unsupervised domain adaptation, in: *European Conference on Computer Vision*, Springer, pp. 597–613.
- Gholipour, A., Estroff, J.A., Warfield, S.K., 2010. Robust super-resolution volume reconstruction from slice acquisitions: application to fetal brain MRI. *IEEE Trans Med Imaging* 29, 1739–1758.
- He, K., Zhang, X., Ren, S., Sun, J., 2015. Deep residual learning for image recognition. *arXiv preprint arXiv:1512.03385*.
- Hoffman, J., Tzeng, E., Park, T., Zhu, J.Y., Isola, P., Saenko, K., Efros, A., Darrell, T., 2018. Cycada: Cycle-consistent adversarial domain adaptation, in: *International conference on machine learning*, PMLR, pp. 1989–1998.
- Huang, X., Liu, M.Y., Belongie, S., Kautz, J., 2018. Multimodal unsupervised image-to-image translation, in: *Proceedings of the European conference on computer vision (ECCV)*, pp. 172–189.
- Kingma, D.P., Ba, J., 2014. Adam: A method for stochastic optimization. *arXiv preprint arXiv:1412.6980*.
- Kingma, D.P., Welling, M., 2013. Auto-encoding variational Bayes. *arXiv preprint arXiv:1312.6114*.
- Kingma, D.P., Welling, M., 2019. An introduction to variational autoencoders. *arXiv preprint arXiv:1906.02691*.
- Ledig, C., Theis, L., Huszár, F., Caballero, J., Cunningham, A., Acosta, A., Aitken, A., Tejani, A., Totz, J., Wang, Z., et al., 2017. Photo-realistic single image super-resolution using a generative adversarial network, in: *Proceedings of the IEEE conference on computer vision and pattern recognition*, pp. 4681–4690.
- Moghari, M.H., Barthur, A., Amaral, M.E., Geva, T., Powell, A.J., 2018. Free-breathing whole-heart 3D cine magnetic resonance imaging with prospective respiratory motion compensation. *Magn Reson Med* 80, 181–189.
- Okta, O., Ferrante, E., Kamnitsas, K., Heinrich, M., Bai, W., Caballero, J., Cook, S.A., De Marvao, A., Dawes, T., O'Regan, D.P., et al., 2017. Anatomically constrained neural networks (ACNNs): application to cardiac image enhancement and segmentation. *IEEE Trans Med Imaging* 37, 384–395.
- Perone, C.S., Ballester, P., Barros, R.C., Cohen-Adad, J., 2019. Unsupervised domain adaptation for medical imaging segmentation with self-ensembling. *NeuroImage* 194, 1–11.
- Petersen, S.E., Matthews, P.M., Francis, J.M., Robson, M.D., Zemrak, F., Boubertakh, R., Young, A.A., Hudson, S., Weale, P., Garratt, S., et al., 2015. UK Biobank's cardiovascular magnetic resonance protocol. *J Cardiovasc Magn Reson* 18, 8.
- Rasti, P., Uiboupin, T., Escalera, S., Anbarjafari, G., 2016. Convolutional neural network super resolution for face recognition in surveillance monitoring, in: *International conference on articulated motion and deformable objects*, Springer, pp. 175–184.
- Rezende, D.J., Mohamed, S., Wierstra, D., 2014. Stochastic backpropagation and approximate inference in deep generative models (2014). *arXiv preprint arXiv:1401.4082*.
- Ronneberger, O., Fischer, P., Brox, T., 2015. U-net: Convolutional networks for biomedical image segmentation, in: *International Conference on Medical image computing and computer-assisted intervention*, Springer, pp. 234–241.
- Sabour, S., Frosst, N., Hinton, G., 2017a. Dynamic routing between capsules. *arXiv preprint arXiv:1710.09829*.
- Sabour, S., Frosst, N., Hinton, G.E., 2017b. Dynamic routing between capsules. *arXiv preprint arXiv:1710.09829*.
- Sánchez, I., Vilaplana, V., 2018. Brain MRI super-resolution using 3D generative adversarial networks. *arXiv preprint arXiv:1812.11440*.
- Savioli, N., de Marvao, A., Bai, W., Wang, S., Cook, S.A., Chin, C.W.L., Rueckert, D., O'Regan, D.P., 2021a. ImperialCollegeLondon/Gemini-GAN. Zenodo doi:10.5281/zenodo.5005942.
- Savioli, N., de Marvao, A., O'Regan, D.P., 2021b. Cardiac super-resolution label maps. Mendeley Data V1. doi:10.17632/pw87p286yx.1.
- Schafer, S., De Marvao, A., Adami, E., Fiedler, L.R., Ng, B., Khin, E., Rackham, O.J., Van Heesch, S., Pua, C.J., Kui, M., et al., 2017. Titin-truncating variants affect heart function in disease cohorts and the general population. *Nat Genet* 49, 46–53.
- Shui, C., Chen, Q., Wen, J., Zhou, F., Gagné, C., Wang, B., 2020. Beyond H-divergence: Domain adaptation theory with Jensen-Shannon divergence. *arXiv preprint arXiv:2007.15567*.
- Tzeng, E., Hoffman, J., Zhang, N., Saenko, K., Darrell, T., 2014. Deep domain confusion: Maximizing for domain invariance. *arXiv preprint arXiv:1412.3474*.
- Wang, M., Deng, W., 2018. Deep visual domain adaptation: A survey. *Neurocomputing* 312, 135–153.
- Wang, Z., Bovik, A.C., Sheikh, H.R., Simoncelli, E.P., 2004. Image quality assessment: from error visibility to structural similarity. *IEEE Trans Image Process* 13, 600–612.
- Woodbridge, M., Fagiolo, G., O'Regan, D.P., 2013. MRIdb: medical image

management for biobank research. *J Digit Imaging* 26, 886–890.

Xia, Y., Ravikumar, N., Greenwood, J.P., Neubauer, S., Petersen, S.E., Frangi, A.F., 2021. Super-resolution of cardiac MR cine imaging using conditional GANs and unsupervised transfer learning. *Med Image Anal* 71, 102037.

Yang, J., An, W., Wang, S., Zhu, X., Yan, C., Huang, J., 2020. Label-driven reconstruction for domain adaptation in semantic segmentation, in: *European Conference on Computer Vision*, Springer. pp. 480–498.

Zhu, J.Y., Park, T., Isola, P., Efros, A.A., 2017a. Unpaired image-to-image translation using cycle-consistent adversarial networks, in: *Proceedings of the IEEE international conference on computer vision*, pp. 2223–2232.

Zhu, J.Y., Zhang, R., Pathak, D., Darrell, T., Efros, A.A., Wang, O., Shechtman, E., 2017b. Toward multimodal image-to-image translation. *arXiv preprint arXiv:1711.11586*.

Zhu, Y., Zhang, Y., Yuille, A.L., 2014. Single image super-resolution using deformable patches, in: *Proceedings of the IEEE Conference on Computer Vision and Pattern Recognition*, pp. 2917–2924.

Appendix A. Theorem 1

In this appendix section, we are going to demonstrate how the VAE loss is given by the combination of Evidence Lower Bound (ELBO) and Kullback-Leibler (KL) divergence and how derivative a gradient forms from it. Indeed, the latent variable z is part of the variational target generator model but we can't directly observe it. In this specific case the direct graphical model is represented by a joint distribution $p_\theta(x; z)$ over both LR input data target volume x and latent variable z . Where, the marginal distribution $p_\theta(x)$, over the observed variable x , is given by:

$$p_\theta(x) = \int p_\theta(x, z) dz \quad (\text{A.1})$$

The θ are the parameters that minimize the integral. However, this marginal distribution $p_\theta(x)$ can be complicated and need to be approximate through a factoring process:

$$p_\theta(x, z) = p_\theta(x) p_\theta(z|x) \quad (\text{A.2})$$

The distribution $p(z)$ is also called prior distribution over latent z variables. The challenge is due to the intractability of $p_\theta(x, z)$, where no analytic solution is given. To solve this intractability, a parametric inference model $q_\phi(z|x)$ is then introduced through an encoder network (i.e., G_ϕ) that optimizes the variational parameters ϕ as $q_\phi(z|x) \approx p_\theta(z|x)$. In the variational inference, this is called lower bound objective (ELBO) optimisation problem (Kingma and Welling, 2019). Then, for any type of parametric inference model $q_\phi(z|x)$, is given:

$$\begin{aligned} \log(p_\theta(x)) &= \mathbb{E}_{q_\phi(z|x)}[\log p_\theta(x)] = \\ &= \mathbb{E}_{q_\phi(z|x)}[\log(\frac{p_\theta(x, z)}{p_\theta(z|x)})] \\ &= \mathbb{E}_{q_\phi(z|x)}[\log(\frac{p_\theta(x, z) q_\phi(z|x)}{q_\phi(z|x) p_\theta(z|x)})] \quad (\text{A.3}) \\ &= \mathbb{E}_{q_\phi(z|x)}[\log(\frac{p_\theta(x, z)}{q_\phi(z|x)})] + \mathbb{E}_{q_\phi(z|x)}[\log(\frac{q_\phi(z|x)}{p_\theta(z|x)})] \end{aligned}$$

The first term, of the last equation line, is the ELBO (i.e., the final variational loss $Loss_{\theta, \phi}(x)$) and is always lower bound for $\log(p_\theta(x))$ (i.e., due to the positive value of the second term).

The ELBO is obtained by substitute the [Eq. A.2] on [Eq. A.3] (i.e., first term of last equation line).

$$Loss_{\theta, \phi}(x) = \mathbb{E}_{q_\phi(z|x)}[\log(\frac{p_\theta(x) p_\theta(z|x)}{q_\phi(z|x)})] \quad (\text{A.4})$$

$$Loss_{\theta, \phi}(x) = \log p_\theta(x) - D_{KL}(q_\phi(z|x) || p_\theta(z|x)) \leq \log p_\theta(x) \quad (\text{A.5})$$

The second term is the Kullback-Leibler (KL) divergence among the parametric inference model $q_\phi(z|x)$ and the marginal distribution $p_\theta(z|x)$ (i.e., also positive):

$$D_{KL}(q_\phi(z|x) || p_\theta(z|x)) = \mathbb{E}_{q_\phi(z|x)}[\log(\frac{q_\phi(z|x)}{p_\theta(z|x)})] \geq 0 \quad (\text{A.6})$$

Finally, we estimate the gradient for both parameters ϕ and θ . In particular for θ we have:

$$\begin{aligned} \nabla_\theta Loss_{\theta, \phi}(x) &= \nabla_\theta \mathbb{E}_{q_\phi(z|x)}[\log(p_\theta(x, z)) - \log(q_\phi(z|x))] \\ &= \mathbb{E}_{q_\phi(z|x)}[\nabla_\theta(\log(p_\theta(x, z)) - \log(q_\phi(z|x)))] \quad (\text{A.7}) \\ &\simeq \nabla_\theta(\log(p_\theta(x, z)) - \log(q_\phi(z|x))) = \nabla_\theta(\log p_\theta(x, z)) \end{aligned}$$

Where the last term of this equation represents the Monte Carlo estimator for z latent variable, randomly sampled from the parametric inference model $q_\phi(z|x)$ (Kingma and Welling, 2013). However, for ϕ parameters there is no valid computational operation between expectation and gradient. Nonetheless, the G_{1_ϕ} encoder is fully differentiable and the latent variable z used continued. Therefore, is calculate the gradient for ϕ variable with a reparameterization step (Rezende et al., 2014). The reparameterization expresses the random variable z in terms of another variable k within a differentiable invertible transformation function $f(\cdot)$. The random noise of the reparameterization variable k is sampled from a univariate Gaussian distribution $\mathcal{N}(0, I)$.

$$z = f(k, \phi, x) \quad (\text{A.8})$$

The random distribution variable k is independent both of the input variable x and the parameter ϕ . In this case the commutation operation between expectation and gradient (i.e., both for the parameters θ and ϕ) is guaranteed. Then, the new Monte Carlo estimator with $z = f(k, \phi, x)$ and random noise sample from $k \sim p(k)$, is given by the following equation:

$$\begin{aligned} \mathbb{E}_{q_\phi(z|x)}[Loss_{\theta, \phi}(z)] &= \mathbb{E}_{p(k)}[Loss_{\theta, \phi}(z)] \\ &= \nabla_\phi \mathbb{E}_{q_\phi(z|x)}[Loss_{\theta, \phi}(z)] \\ &= \mathbb{E}_{p(k)}[\nabla_\phi Loss_{\theta, \phi}(z)] \\ &\simeq \nabla_\phi Loss_{\theta, \phi}(z) \quad (\text{A.9}) \end{aligned}$$

After the reparameterization trick:

$$\begin{aligned} k &\sim \mathcal{N}(0, I) \\ (\mu_t, \log \sigma_t) &= \text{Encoding}_{G_{1_\phi}}(x) \quad (\text{A.10}) \\ z &= \mu_t + \sigma_t \odot k \end{aligned}$$

Given the $q_\phi(z|x)$ is Gaussian and is approximate by $Encoding_{G_{x\phi}}$, the final inference is given by:

$$\begin{aligned} (\mu_x, \log(\sigma_x)) &= Encoding_{G_{x\phi}}(I_x) \\ q_\phi(z_x|I_x) &= \mathcal{N}(z_x; \mu_x, diag(\sigma_x)) \end{aligned} \quad (A.11)$$

Where I_x indicated a general input image, $Encoding_{G_{x\phi}}$ a generic encoding network, z_x a generic latent variables of $Encoding_{G_{x\phi}}$, and μ_x, σ_x the generic mean and standard deviation (i.e., predicted by $Encoding_{G_{x\phi}}$) of the Gaussian distribution $\mathcal{N}(z_x; \mu_x, diag(\sigma_x))$, k is the index of the sum operation. We can then conclude

$$\begin{aligned} \log(q_\phi(z_x|I_x)) &= \sum_k \log(\mathcal{N}(z_{x_k}, 0, 1)) - \log(\sigma_{x_k}) \\ &= \sum_k \frac{1}{2} (\log(\sigma_{x_k}) - \mu_{x_k}^2 - \sigma_{x_k}^2 + 1) \end{aligned} \quad (A.12)$$

Appendix B. Theorem 2

In this appendix section, we are going to demonstrate that if the variational generator $G_{t\phi}$ and its discriminator D_t are enough numerically stable, at each step iteration, the discriminator D_t reach its optimum where the target output probability $p_t^*(x)$ of I_t^* converges to the target data I_t UKDHP distribution probability $p_t(x)$. Then, if we set $K(p_t^*(x), D_t)$ a function of the “fake” target probability distribution generate by $G_{t\phi}$, the function $K(p_t^*(x), D_t)$ shows a convexity in this “fake” probability distribution $p_t^*(x)$.

To prove this, we let:

$$K(p_t^*(x), D_t) = \sup_\alpha K_\alpha(p_t^*(x), D_t) \quad (B.1)$$

Where the function $K_\alpha(p_t^*(x), D_t)$ are convex on some convex domain S . We suppose that at particular point $p_t^*(x)$ in S ,

$$\beta = \operatorname{argsup}_\alpha K_\alpha(p_t^*(x), D_t) \quad (B.2)$$

Then,

$$K(p_t^*(x), D_t) = K_\beta(p_t^*(x), D_t) \quad (B.3)$$

Let m be any subgradient of $K_\beta(p_t^*(x), D_t)$, for definition of subgradient,

$$K_\beta(p_t^*(y), D_t) \geq K_\beta(p_t^*(x), D_t) + m^T(y - x) \quad (B.4)$$

Since $K(p_t^*(y), D_t) \geq K_\beta(p_t^*(x), D_t)$ for $y \in S$,

$$K(p_t^*(y), D_t) \geq K(p_t^*(x), D_t) + m^T(y - x) \quad (B.5)$$

Thus, we have $m \in \partial K(p_t^*(x), D_t)$, but also for any subgradient $\partial K_\beta(p_t^*(x), D_t) \in \partial K(p_t^*(x), D_t)$. This is equivalent to calculate any update of Stochastic Gradient Descent (SDG) for $p_t^*(x)$ at the optimal discriminator value $D_t^{optim}(x)$, given the variational generator $G_{t\phi}$, to observed that any small update of generative “fake” distribution $p_t^*(x)$ and UKDHP data “real” distribution $p_t(x)$ converges to the data “real” distribution $p_t^*(x)$; as $\sup_{D_t^{optim}(x)} K(p_t^*(x), D_t^{optim}(x))$ is convex in $p_t^*(x)$, $p_t^* \rightarrow p_t(x)$, concluding the proof.